Characteristic form and distance in high-level hierarchical structure of self-aggregated clouds in radiative-convective equilibrium

Tomoro Yanase[1,2], Seiya Nishizawa[2], Hiroaki Miura[3,2], and Hirofumi Tomita[2,1]

[1]RIKEN Cluster for Pioneering Research, Kobe, Japan

[2]RIKEN Center for Computational Science, Kobe, Japan

[3]Graduate School of Science, The University of Tokyo, Tokyo, Japan

Corresponding author: Tomoro Yanase (tomoro.yanase@riken.jp)

Key Points:

- Convective self-aggregation was studied using cloud-resolving simulations, increasing the domain sizes up to approximately 25,000 km.
- The characteristic horizontal scale of column moisture converges to 3,000–4,000 km in a domain larger than 5,000 km.
- The cloud aggregation area takes a mesh-like form in the quasi-equilibrium stage and a circular form in the transient stage.

Abstract

The nature of convective organization remains elusive, despite its importance for understanding the role of clouds in climate systems. This study reports a new type of large-scale structure formed by the self-organization of deep moist atmospheric convection in radiative-convective equilibrium. To understand the natural behavior of convection unaffected by the computational domain, we conducted cloud-resolving simulations by systematically increasing the horizontal domain size to approximately 25,000 km. We found that if the domain side length exceeded 5,000 km, the domain-averaged thermodynamic fields and the horizontal characteristic length converged in quasi-equilibrium; the cloud aggregation area exhibited a mesh-like pattern, analogous to the shallow convective organizations despite their different scales. Its characteristic length is estimated to be approximately 3,000–4,000 km. The results suggest that this length scale is related to the upper-limit size of mesoscale convective systems or the scale of supercloud clusters in a real tropical atmosphere.

Plain Language Summary

Tropical deep convective storms often gather to form large-scale phenomena, such as cloud clusters. However, the preferred horizontal scales and patterns in the large-scale self-organization of convection are not well understood. This study investigated the spontaneous scale selection of deep convection by conducting idealized radiative-convective simulations with an unprecedented broad computational domain with a side length of over 10,000 km. When the domain size was sufficiently large, the large-scale fields of moisture and clouds had a characteristic horizontal scale of approximately 3,000–4,000 km with a mesh-like organization pattern. Although the simulations were performed under idealized conditions, this discovery will provide new insight into the fundamental physical mechanisms that control the spatial scale and pattern of convective clusters in a real-world tropical atmosphere.

1 Introduction

Cumulus convection is often organized into large-scale systems, such as mesoscale convective systems (Houze, 2004; Robe & Emanuel, 2001), tropical cyclones (Nolan et al., 2007; Ritchie & Holland, 1999), and the Madden-Julian Oscillation (MJO; Madden & Julian, 1971, 1972; Zhang, 2005; Miura et al., 2007, 2009). Tropical cumulus clouds often have hierarchical structures (Nakazawa, 1988). The higher-level hierarchies have a horizontal scale of several thousand kilometers coupled with equatorial waves (Kiladis et al., 2009).

To understand the cloud systems modulated by the external environment, it is necessary to investigate the intrinsic characteristics of cloud organization, which have been studied by simulating radiative-convective equilibrium (RCE) using explicitly represented convection models (Held et al., 1993; Tompkins & Craig, 1998; Bretherton et al., 2005; Muller & Held, 2012; Patrizio & Randall, 2019, hereafter PR19; Yanase et al., 2018, 2020). The spontaneous organization of clouds in RCE, commonly referred to as convective self-aggregation (CSA), has received increasing attention in recent years (Wing et al., 2017; Muller et al., 2022). Although researchers have studied various aspects of CSA, it is not yet understood what horizontal form and scale CSA prefers and what mechanisms are responsible for determining them.

Using cloud-resolving models (CRMs) on square domains with periodic boundary conditions, past studies reported that clouds are organized into a single cluster with circular, banded, or more complex horizontal shapes (Bretherton et al., 2005; PR19; Yanase et al., 2020).

Note that when a single organization is represented in the computational domain, its horizontal scale and shape may be affected by the domain size (PR19). To discuss the natural horizontal scale of CSA and its physical reason, it is necessary for multiple organizations to appear by widening the computational domain. Simultaneously, the domain-mean statistics should converge against the domain size. For example, PR19 conducted a series of RCE experiments by varying the domain size from 768 to 6,144 km. Their results showed that, whereas a single convective cluster formed in a domain size smaller than 3,000 km, two semi-connected bands appeared in the domain size of over 6,000 km. Based on the qualitative change in the large-scale horizontal shapes of convective clusters between the 3,072-km and 6,144-km domains, PR19 cautioned that the natural spatial scale of CSA existed around these domain sizes. However, domain-mean statistics, such as precipitable water (PW), did not converge with respect to the domain size, even between 3,072-km and 6,144-km runs. This suggests the necessity of a larger domain for the numerical convergence of the CSA characteristics.

When CRMs were used on regional elongated channel domains (e.g., Wing & Cronin, 2016) or two-dimensional (x, z) domains (e.g, Yang, 2018, hereafter Y18), CSA took multiple band shapes. Y18 proposed a scaling theory for the horizontal scale of CSA by focusing on planetary boundary layer (PBL) dynamics. His theory supported his simulation results in that the horizontal CSA scale became 2,000 km. However, because the two-dimensional framework possibly restricts the behavior of moist convection, the extent to which this theory is applicable to explain the horizontal scale of CSA in three-dimensional simulations remains unclear. Moreover, if the three-dimensional domain is sufficiently large to contain multiple clusters, it remains unknown whether clusters take a band-like form or other forms (e.g., circular form).

In addition to CRMs simulations, several studies have used low-resolution models with parameterized convection to facilitate large-scale (~10,000 km) square-domain simulations of RCE (Silvers et al., 2016; Arnold & Putman, 2018). Arnold and Putman (2018) systematically increased the domain size from 1,000 to 10,000 km, showing that, whereas a single circular humid cluster formed with a domain size shorter than approximately 5,000 km, the humid region could broke into multiple clusters when the domain size was approximately 10,000 km. This result is consistent with the examination of the domain size dependence in PR19. Nevertheless, a recent model intercomparison study revealed that models with different convective parameterizations result in various cloud organizations (Wing et al., 2020). Moreover, even if the same convective parameterization was used, the change in the parameterization parameter affected the convective organization (Becker et al., 2017). To avoid the uncertainty inherent in the convective parameterization problem (Arakawa, 2004) and to facilitate the comparison with the counterpart study (PR19), this study performed RCE experiments using CRM.

This study aims to clarify what form and scale in the horizontal direction are preferred for the large-scale self-organization of moist convection. For this purpose, the influence of the domain size should be avoided as much as possible. Based on the results from PR19, which did not converge even with a domain size of 6,000 km, we drastically extended the domain size to investigate the domain size required for convergence and what kind of large-scale structure is formed. In addition, based on the scaling theory proposed by Y18, we determine the physical quantities that contribute to the convergence of the CSA length scale with respect to the domain size.

2 Methods

We conducted a series of CSA numerical experiments using a regional CRM called SCALE-RM version 5.3.3 (Nishizawa et al., 2015; Sato et al., 2015). To examine the dependence of CSA on the size of horizontally periodic square three-dimensional computational domains, we systematically increased the horizontal domain size by doubling from 768 to 24,576 km. The horizontal grid spacing was 8 km and the time step was 24 s for all runs. The integration times were 200 d for the 768-, 1,536-, 3,072-, and 6,144-km domain runs (hereafter, L768, L1536, L3072, and L6144) and 150 d for the 12,288- and 24,576-km domain runs (hereafter, L12288 and L24576). Other experimental setups of the boundary conditions and physical parameterizations described below were the same as those of Yanase et al. (2020), the one-moment bulk microphysics scheme (Tomita, 2008), the first-order closure sub-grid scale turbulence scheme (Brown et al., 1994; Scotti et al., 1993), the bulk surface flux scheme (Beljaars & Holtslag, 1991; Wilson, 2001), and the broadband radiative transfer scheme (Sekiguchi & Nakajima, 2008). These configurations follow Tompkins and Craig (1998) and Muller and Held (2012). The top of the model was 24 km with 64 layers. The sea surface temperature (SST) at the lower boundary was fixed at 300 K. The initial thermodynamic profiles of potential temperature and specific humidity were obtained by another 100-day run from a tropical sounding profile on the 96-km domain at a 2-km horizontal resolution (Yanase et al., 2020).

3 Results

Figure 1 shows the horizontal distribution of PW and outgoing longwave radiation (OLR) on the 50th and last days. In the two smallest domain runs (L768, L1536), the moist-cloudy regions with high PW and low OLR values were organized into single circular patches (Figs. 1a,b,g,h). These organizations are similar to those obtained by several previous RCE studies using cloud-resolving models in square domains (e.g., Fig. 3 of Bretherton et al., 2005; Figs. 2b,d of Muller & Held, 2012; Fig. 1b: Wing & Emanuel, 2014; Fig. 2c: Ruppert & Hohenegger, 2018; Fig. 2a: PR19; Fig. 1a: Windmiller & Hohenegger, 2019). We also observed that the horizontal size of the moist patch increased proportionally with the domain size. Hence, the length scales of these organizations in small domains are restricted by the computational domain configuration and are considered different from the natural scale (PR19). In the run on the third smallest area (L3072; Figs. 2c and i), the moist-cloudy region was organized into a single patch, as in the smaller domain runs (L768, L1536). However, the horizontal form of the moist patch was not circular in quasi-equilibrium, but band shape (right panel of Fig. 1c). This organization is consistent with several previous studies (e.g., Fig. 6 of Tompkins & Craig, 1998; Figs. 1j–m of Muller & Bony, 2015).

There was only a single moist patch in the smaller domains (Figs. 1a–c and 1 g–i), whereas multiple patches coexisted during the transient phase in L6144 (left panels of Figs. 1d,j). This suggests that the proportional relationship between the moist patch and domain sizes begins to break at L6144. In the quasi-equilibrium phase of L6144, multiple moist patches were aggregated, whereas the organization took a complex shape rather than single circle or band shape (right panels of Figs. 1d,j). In the quasi-equilibrium phase of L12288 (Figs. 1e and k), there was a mesh-like organization that is very similar to that of the vertical velocity field seen in the boundary layer dry convection (e.g., Fig. 3a of Nishizawa et al., 2015) or the open cellular organization of shallow convective cloud fields (e.g., Fig. 2 of Yamaguchi & Feingold, 2015). It is interpreted that a piece of the mesh-like organization in L12288 was partially resolved in the smaller domains, as seen in the complex shape in L6144 (Fig. 1d) and the two semi-connected bands of PR19. Finally, the largest domain run (L24576 in Figs. 1f and l) showed a mesh-like large-scale organization similar to that of L12288. The pattern seen in a quarter section of L24576 is equivalent to that in L12288, and the characteristic horizontal length scales of these organizations are identical. In short, such a selection of mesh-like structures with a specific characteristic length can be observed if the domain size exceeds 5,000 km.

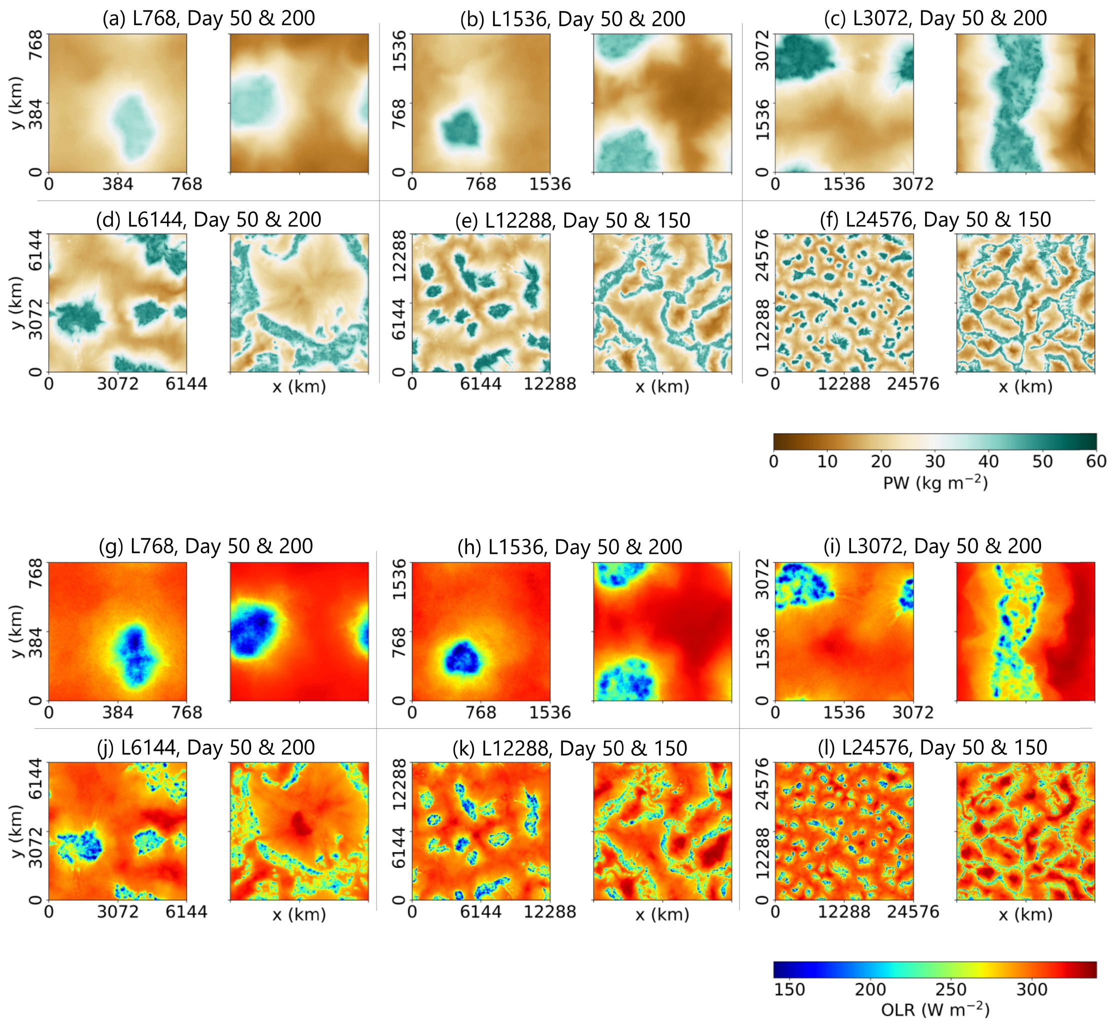

Figure 1. Horizontal distributions of daily mean precipitable water (a)–(f) and outgoing longwave radiation (g)–(l) on day 50 and the last day, in six runs: (a),(g) L768 , (b),(h) L1536, (c),(i) L3072 , (d),(j) L6144 , (e),(k) L12288 , and (f),(l) L24576.

To compare the climatology among the different domain runs, Figure 2 shows the time evolutions of the daily horizontal mean values of PW and OLR. Figure 2a shows that PW decreases with time for all runs for approximately 30 days from the start of integration, which is consistent with previous findings that the development of CSA is associated with domain-mean drying (Wing et al., 2017). Subsequently, the time variation of PW increased. In the quasi-equilibrium phase (defined as the period after day 60), the mean value generally increased with the domain size and converged to approximately 28 kg m^{-2} in L6144, L12288, and L24576 (Fig. 2c). The OLR showed the opposite temporal change to PW (Fig. 2b). This result can be understood by the rising height of the effective emission of longwave radiation and the decrease in brightness temperature with an increase in the amount of water vapor. The quasi-equilibrium value for the OLR converged to approximately 284 W m^{-2} (Fig. 2d). Although PR19 could not confirm the convergence of the domain-mean value with respect to the domain size, our results showed that the values of L6144 almost reached the same magnitude as the larger domain runs.

Moreover, slow temporal oscillations were observed in domain-mean values. In particular, in both PR19 and L3072 runs showed oscillation with a similar period of approximately 30 days. According to the analysis by PR19, this slow oscillation is an oscillation between the congestus and deep convective phases, where static stability and humidity play central roles. In addition, we found another slower oscillation with a period of approximately 120 days in L6144, which can be roughly estimated as the time interval between days 80 and 200, where the PW values were the same (30 kg m^{-2}). Whether the physical mechanism of this newly found 120-day oscillation is analogous to that of the 30-day oscillation should be investigated in future studies. These slow oscillations were not clearly identified in larger domain runs (L12288 and L24576). As shown in Fig. 1, L12288 and L24576 contain multiple organizational units of the mesh-like large-scale structure, whereas L6144 only marginally contains a single organizational unit of the large-scale system. It is speculated that the phase differences in the periodic fluctuation of organization units cancel each other owing to the wide domain mean. This is why the slow oscillation becomes unclear in larger-domain runs.

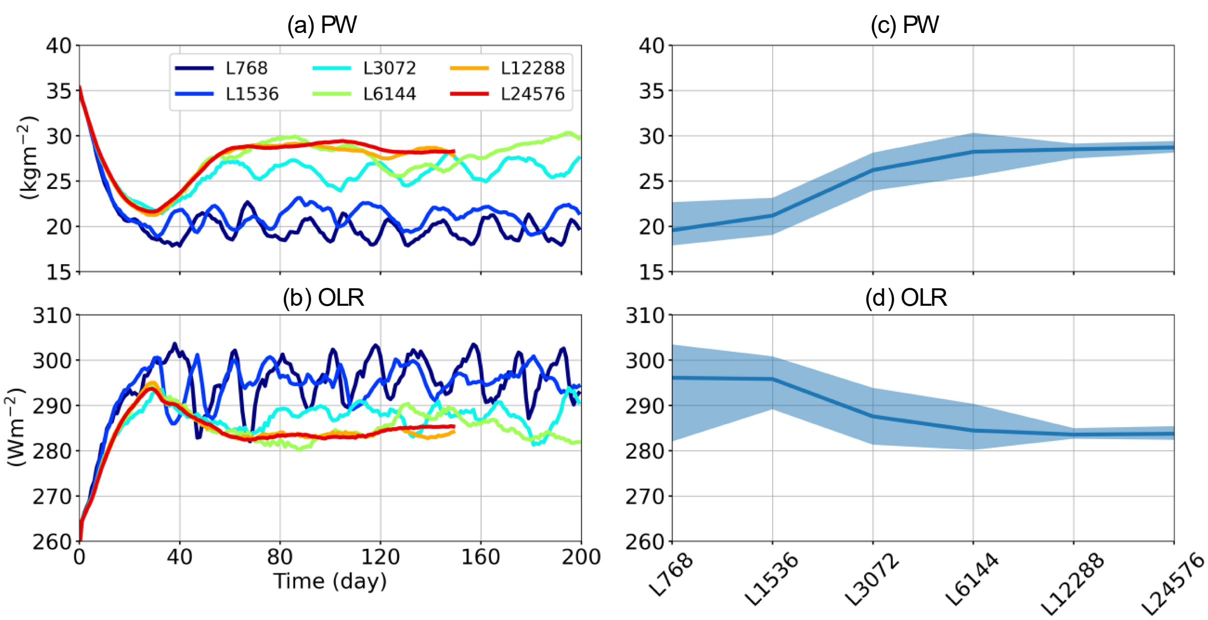

Figure 2. Time evolution of the daily horizontal mean values of PW (a) and OLR (b) and the changes in their quasi-equilibrium values with respect to the domain size (c),(d). The quasi-equilibrium phase is defined as the period after 60 days from the start of integration. The solid lines in (c),(d) indicate the temporal mean in the quasi-equilibrium phase and the shaded areas in

(c),(d) indicate the minimum and maximum ranges of the temporal change in the quasi-equilibrium phase.

To quantify the characteristic horizontal scale of the large-scale organizational structure and its convergence with respect to the domain size, Figure 3 shows the horizontal power spectral density (PSD) $\phi_{\mathrm{PW}}(k_h)$, which was obtained from the two-dimensional field of PW following Durran et al. (2017). $k_h = \sqrt{k_x^2 + k_y^2}$ is the total horizontal wavenumber and k_x and k_y are the horizontal wavenumbers in the x and y directions, respectively. The PSD generally increased from the shortest to the longer horizontal wavelength. In the two largest domain runs (L12288 and L24576), the PSD peaked at horizontal wavelengths of several thousand kilometers and decreased at larger horizontal wavelengths. We also defined the PSD-weighted horizontal wavelength (e.g., Tomita & Abe, 2000; Beucler & Cronin, 2019):

$$\lambda_{\mathrm{PW}} = \frac{\sum \frac{2\pi}{k_h} \phi_{\mathrm{PW}}(k_h)}{\sum \phi_{\mathrm{PW}}(k_h)}.$$

The PSD-weighted wavelength increased with the domain size in the quasi-equilibrium phase and converged toward approximately 3,000–4,000 km in the largest three runs (Fig. 3b).

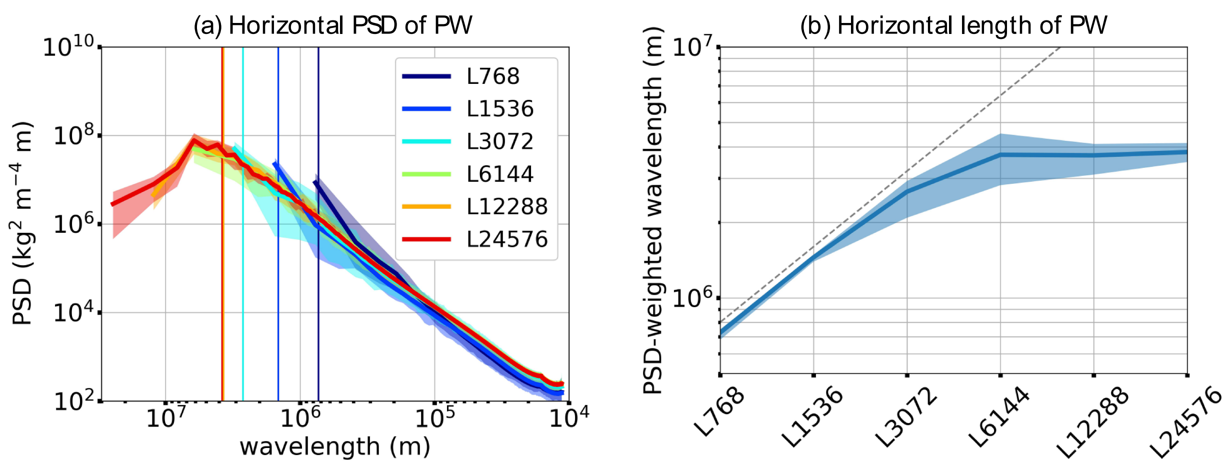

Figure 3. (a) Horizontal power spectral density of PW in quasi-equilibrium. The vertical lines are the PSD-weighted horizontal wavelengths of PW. (b) Change in the PSD-weighted horizontal wavelengths of PW with respect to the domain size; the dashed line is the identity line. The shaded vertical ranges in (a),(b) indicate the minimum and maximum ranges of the temporal change in quasi-equilibrium.

To provide physical insights into the large-scale organization of moist convection, we diagnosed the horizontal scale of the organization using a theory of CSA length scale by Y18 based on a steady-state linear Boussinesq equation system integrated over the PBL and a weak temperature gradient approximation at the PBL top. Y18 showed that the horizontal wavelength of CSA λ can be written as follows:

$$\lambda = \beta h \left\langle \frac{\delta\rho}{\rho_0} \right\rangle_{\mathrm{PBL}}^{\frac{1}{2}},$$

where $\beta = \pi(2g\tau s_T/\langle\delta Q\rangle_{\mathrm{LFT}})^{1/2}$ is a non-dimensional parameter, h is the PBL depth, $\langle\delta\rho/\rho_0\rangle_{\mathrm{PBL}}$ is the amplitude of the fractional density horizontal anomaly in the PBL, $\delta\rho$ is the amplitude of the horizontal density anomaly, ρ_0 is the horizontal mean density, g is the gravitational acceleration, τ is the damping time scale for the horizontal velocity in the PBL, $s_T \equiv \langle(\mathrm{d}s/\mathrm{d}z)/c_p\rangle_{\mathrm{LFT}}$ is the static stability in the lower free troposphere (LFT), s is the dry static energy, c_p is the constant pressure specific heat of air, and $\langle\delta Q\rangle_{\mathrm{LFT}}$ is the horizontal anomaly of diabatic heating in the LFT. The amplitude was defined as half the difference between the values in the moist (upper 25% PW subdomain) and dry (upper 25% PW subdomain) regions. The top height of the PBL was defined as the altitude at which the virtual potential temperature first exceeded the values at the lowest model level. The LFT was defined as the layer between the PBL top height and double the PBL top height. τ is treated as a constant for one day following Y18.

Figure 4 shows the domain-size dependencies of the estimated characteristic horizontal wavelength and related physical quantities based on the scaling theory above. The estimated length increased with domain size and converged to approximately 2,000 km (Fig. 4a). This convergence qualitatively reproduces the same order of magnitude as that of the PSD-weighted length based on the PW fields. As the domain size increased from the smallest to the largest, the PBL height decreased by approximately 20%, contributing to the shortening of the CSA horizontal length (Fig. 4b). The square root of the buoyancy amplitude increased by approximately 180% and contributed to the extension of the CSA horizontal length (Fig. 4c). The diabatic heating amplitude and static stability in the LFT increased by approximately 40% and 70%, respectively. As they almost compensate, the increase in β was less than 10% (Fig. 4d). The above diagnosis suggests that buoyancy in the PBL largely contributes to the CSA length scale, although the change in the variables above may not be physically independent.

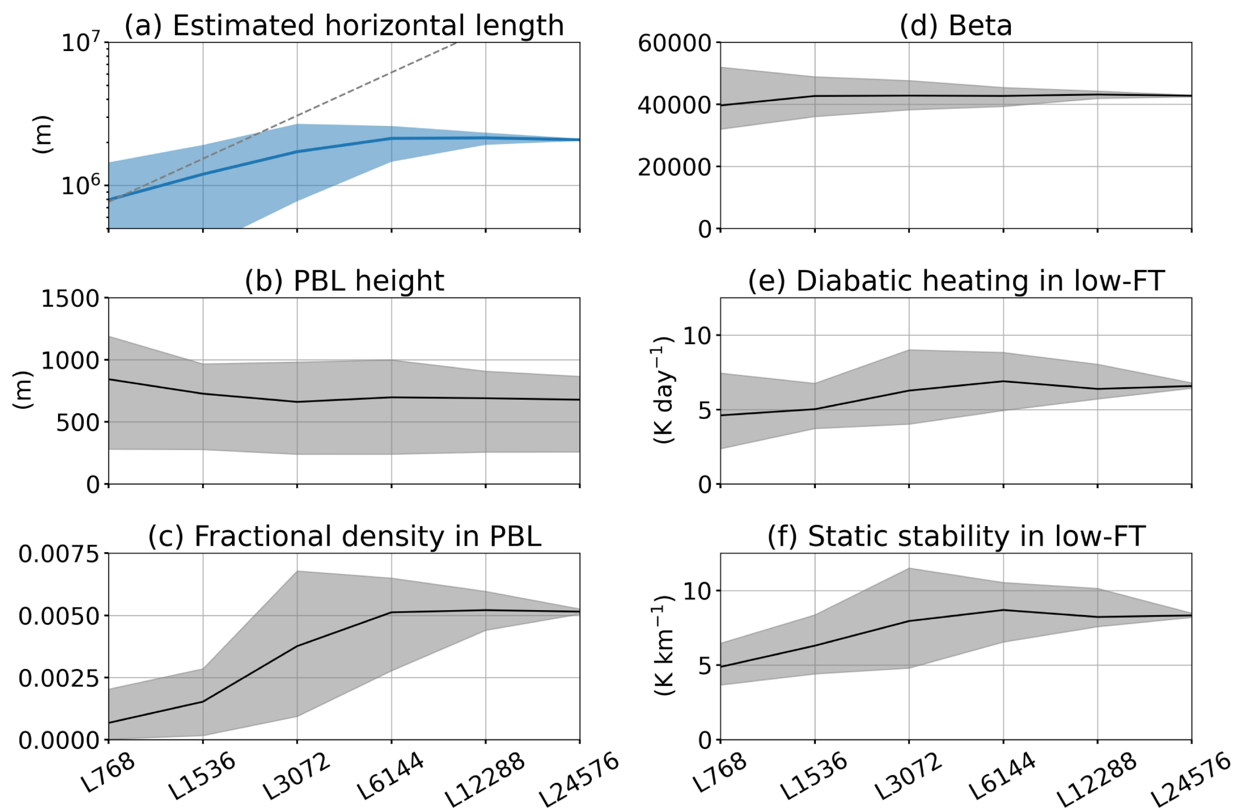

Figure 4. (a) Horizontal length of CSA diagnosed based on Y18's scaling theory. (b) PBL height. (c) The amplitude of fractional density anomaly in the PBL. (d) Nondimensional parameter relating horizontal length of CSA, PBL depth, and amplitude of buoyancy anomaly in PBL. (e) Amplitude of diabatic heating in the LFT. (f) Static stability in the LFT. The shades indicate the minimum and maximum ranges of the temporal change in quasi-equilibrium. Due to the limit of computational resources, the L24576 case was evaluated for the final 20 days.

5 Conclusion and perspectives

To investigate the characteristic form and horizontal scale of the spontaneously formed moist convective organization in the RCE, we conducted a series of large-domain numerical experiments that simultaneously resolved individual deep convective clouds and large-scale structures. The 10,000-km scale simulations revealed that, although the large-scale organization of the aggregated cloud area took multiple circular forms in the transient phase, a mesh-like structure appeared in the quasi-equilibrium phase. The domain-mean climate almost converged on a domain larger than 5,000 km and the characteristic horizontal wavelength of the organization was 3,000–4,000 km.

To understand the role of convective organization, further examination is needed to clarify why the moist atmosphere selects the mesh-like structure under RCE as the idealized essential climate state. By analogy with the selection of roll and hexagonal patterns in the Bénard–Marangoni convection (e.g., Tomita & Abe, 2000), a clue would be to identify how different organizations achieve the energy transformation associated with large-scale moist convection. One straightforward approach is to compare the mesh-like organization in the square domain (e.g., the quasi-equilibrium phase of L12288) and the band-like organization in the elongated channel domain. This is important for the selection of a large-scale moist convection organization. We showed that the scaling theory by Y18 served as a useful constraint relating to the horizontal scale of the organization, buoyancy in the PBL, and PBL depth. However, the framework does not explain why a horizontal scale is preferentially selected. Identifying how energy transformation depends on the horizontal scale of the organization will deepen our understanding of the physical basis of moist convective organization.

Matsugishi and Satoh (2022) conducted global RCE experiments and showed that the planetary radius must not be smaller than half of Earth's radius for the convergence of domain-mean statistics and the representation of multiple aggregated clusters. Their results were consistent with those of PR19 and our results using regional models. However, the mesh-like large-scale organization found in our study did not appear in the global domain runs. Currently, it is indistinguishable whether this difference is due to differences in the domain topology, other experimental setups, or model formulations, including physical parameterizations. To clarify the effect of domain topology on the morphology of the large-scale organization of moist convection, careful comparisons by changing only the domain topology are needed; the model formulations (i.e., the scheme of dynamical core and physical parameterizations including their parameters) should be the same in the two cases.This issue will be addressed in future studies.

Regarding the relationship between CSA and convective organization in the real world, Beucler et al. (2019) pointed out the similarity between RCE experiments on an elongated channel domain and the tropical atmosphere near the equator from the viewpoint of moist static energy (MSE) variability. There were several common characteristics across the idealized models and real-world data: radiation amplified the MSE variability at larger horizontal scales, surface fluxes damped the variability at larger horizontal scales, and advection damped the variability at almost all horizontal scales. However, there was a significant difference: PSD increased monotonically from the shortest to the longest horizontal wavelength in the real world, whereas PSD exhibited a peak at several thousands of kilometers in the idealized experiments. Beucler et al. (2019) suggested that the amplification effect of vertical advection may play a role in the formation of a PSD peak at a specific horizontal scale in the RCE. Satoh et al. (2016) discussed the difference between convection systems in aquaplanet experiments and RCE experiments in terms of horizontal propagation and vertical tilting characteristics. Combining the above two perspectives, the vertically resolved MSE variance budget framework of Yao et al. (2022) can provide a helpful analysis method. As Y18 suggested, further examination of the CSA scale may provide insights into the physical mechanism controlling the largest size of mesoscale convective systems and cloud clusters in the tropics, along with the length scales modulated by planetary rotation and radius (Chavas & Reed, 2019).

To understand how moist convective organization impacts global thermodynamically constrained systems, such as global climate, it is necessary to investigate the form and length scale that moist convection prefers across a hierarchy of models and conditions (e.g., Jeevanjee et al., 2017; Maher et al. 2019), such as boundary (e.g., SST; Müller & Hohenegger, 2020) and dynamic (e.g., planetary rotation; Chavas & Reed, 2019) forcings.

Acknowledgments

This work was supported by JSPS KAKENHI (grant number JP19H01974). The RIKEN Junior Research Associate Program and RIKEN Special Postdoctoral Researcher Program supported Tomoro Yanase. The numerical simulations were conducted at Fugaku, RIKEN Center for Computational Science, and the supercomputer of ACCMS, Kyoto University. The authors appreciate Team SCALE for providing SCALE-RM version 5.3.3.

Data Availability Statement

The SCALE library used in this study is publicly available (https://scale.riken.jp/).

References

Arakawa, A. (2004). The cumulus parameterization problem: Past, present, and future. *Journal of Climate*, *17*(13), 2493–2525. https://doi.org/10.1175/1520-0442(2004)017<2493:RATCPP>2.0.CO;2

Arnold, N. P., & Putman, W. M. (2018). Nonrotating convective self-aggregation in a limited area AGCM. *Journal of Advances in Modeling Earth Systems*, *10*(4), 1029–1046. https://doi.org/10.1002/2017MS001218

Becker, T., Stevens, B., & Hohenegger, C. (2017). Imprint of the convective parameterization and sea-surface temperature on large-scale convective self-aggregation. *Journal of Advances in Modeling Earth Systems*, *9*(2), 1488–1505. https://doi.org/10.1002/2016MS000865

Beljaars, A. C. M., & Holtslag, A. A. M. (1991). Flux parameterization over land surfaces for atmospheric models. *Journal of Applied Meteorology*, *30*(3), 327–341. https://doi.org/10.1175/1520-0450(1991)030<0327:FPOLSF>2.0.CO;2

Beucler, T., & Cronin, T. (2019). A budget for the size of convective self-aggregation. *Quarterly Journal of the Royal Meteorological Society*, *145*(720), 947–966. https://doi.org/10.1002/qj.3468

Beucler, T., Abbott, T. H., Cronin, T. W., & Pritchard, M. S. (2019). Comparing convective self-aggregation in idealized models to observed moist static energy variability near the equator. *Geophysical Research Letters*, *46*(17–18), 10589–10598. https://doi.org/10.1029/2019GL084130

Bretherton, C. S., Blossey, P. N., & Khairoutdinov, M. (2005). An energy-balance analysis of deep convective self-aggregation above uniform SST. *Journal of the Atmospheric Sciences*, *62*(12), 4273–4292. https://doi.org/10.1175/JAS3614.1

Brown, A. R., Derbyshire, S. H., & Mason, P. J. (1994). Large-eddy simulation of stable atmospheric boundary layers with a revised stochastic subgrid model. *Quarterly Journal of the Royal Meteorological Society*, *120*(520), 1485–1512. https://doi.org/10.1002/qj.49712052004

Chavas, D. R., & Reed, K. A. (2019). Dynamical aquaplanet experiments with uniform thermal forcing: System dynamics and implications for tropical cyclone genesis and size. *Journal of the Atmospheric Sciences*, *76*(8), 2257–2274. https://doi.org/10.1175/JAS-D-19-0001.1

Durran, D., Weyn, J. A., & Menchaca, M. Q. (2017). Practical considerations for computing dimensional spectra from gridded data. *Monthly Weather Review*, *145*(9), 3901–3910. https://doi.org/10.1175/MWR-D-17-0056.1

Held, I. M., Hemler, R. S., & Ramaswamy, V. (1993). Radiative-convective equilibrium with explicit two-dimensional moist convection. *Journal of the Atmospheric Sciences*, *50*(23), 3909–3927. https://doi.org/10.1175/1520-0469(1993)050<3909:RCEWET>2.0.CO;2

Houze, R. A. (2004). Mesoscale convective systems. *Reviews of Geophysics*, *42*(4). https://doi.org/10.1029/2004RG000150

Jeevanjee, N., Hassanzadeh, P., Hill, S., & Sheshadri, A. (2017). A perspective on climate model hierarchies. *Journal of Advances in Modeling Earth Systems*, *9*(4), 1760–1771. https://doi.org/10.1002/2017MS001038

Kiladis, G. N., Wheeler, M. C., Haertel, P. T., Straub, K. H., & Roundy, P. E. (2009). Convectively coupled equatorial waves. *Reviews of Geophysics*, *47*(2), RG2003. https://doi.org/10.1029/2008RG000266

Madden, R. A., & Julian, P. R. (1971). Detection of a 40–50 day oscillation in the zonal wind in the tropical pacific. *Journal of the Atmospheric Sciences*, *28*(5), 702–708. https://doi.org/10.1175/1520-0469(1971)028<0702:DOADOI>2.0.CO;2

Maher, P., Gerber, E. P., Medeiros, B., Merlis, T. M., Sherwood, S., Sheshadri, A., et al. (2019). Model hierarchies for understanding atmospheric circulation. *Reviews of Geophysics*, *57*(2), 250–280. https://doi.org/10.1029/2018RG000607

Matsugishi, S., & Satoh, M. (2022). Sensitivity of the horizontal scale of convective self-aggregation to sea surface temperature in radiative convective equilibrium experiments using a global nonhydrostatic model. *Journal of Advances in Modeling Earth Systems*, *14*(5), e2021MS002636. https://doi.org/10.1029/2021MS002636

Miura, H., Satoh, M., Nasuno, T., Noda, A. T., & Oouchi, K. (2007). A Madden-Julian oscillation event realistically simulated by a global cloud-resolving model. *Science*, *318*(5857), 1763–1765. https://doi.org/10.1126/science.1148443

Miura, H., Satoh, M., & Katsumata, M. (2009). Spontaneous onset of a Madden-Julian oscillation event in a cloud-system-resolving simulation. *Geophysical Research Letters*, *36*(13), L13802. https://doi.org/10.1029/2009GL039056

Muller, C., & Bony, S. (2015). What favors convective aggregation and why?. *Geophysical Research Letters*, *42*(13), 5626–5634. https://doi.org/10.1002/2015GL064260

Muller, C., Yang, D., Craig, G., Cronin, T., Fildier, B., Haerter, J. O., et al. (2022). Spontaneous aggregation of convective storms. *Annual Review of Fluid Mechanics*, *54*(1), 133–157. https://doi.org/10.1146/annurev-fluid-022421-011319

Muller, C. J., & Held, I. M. (2012). Detailed Investigation of the self-aggregation of convection in cloud-resolving simulations. *Journal of the Atmospheric Sciences*, *69*(8), 2551–2565. https://doi.org/10.1175/JAS-D-11-0257.1

Müller, S. K., & Hohenegger, C. (2020). Self-aggregation of convection in spatially varying sea surface temperatures. *Journal of Advances in Modeling Earth Systems*, *12*(1). https://doi.org/10.1029/2019MS001698

Nakazawa, T. (1988). Tropical super clusters within intraseasonal variations over the western pacific. *Journal of the Meteorological Society of Japan. Ser. II*, *66*(6), 823–839. https://doi.org/10.2151/jmsj1965.66.6_823

Nishizawa, S., Yashiro, H., Sato, Y., Miyamoto, Y., & Tomita, H. (2015). Influence of grid aspect ratio on planetary boundary layer turbulence in large-eddy simulations. *Geoscientific Model Development*, *8*(10), 3393–3419. https://doi.org/10.5194/gmd-8-3393-2015

Nolan, D. S., Rappin, E. D., & Emanuel, K. A. (2007). Tropical cyclogenesis sensitivity to environmental parameters in radiative-convective equilibrium. *Quarterly Journal of the Royal Meteorological Society*, *133*(629), 2085–2107. https://doi.org/10.1002/qj.170

Patrizio, C. R., & Randall, D. A. (2019). Sensitivity of convective self-aggregation to domain size. *Journal of Advances in Modeling Earth Systems*, *11*(7), 1995–2019. https://doi.org/10.1029/2019MS001672

Ritchie, E. A., & Holland, G. J. (1999). Large-scale patterns associated with tropical cyclogenesis in the western pacific. *Monthly Weather Review*, *127*(9), 2027–2043. https://doi.org/10.1175/1520-0493(1999)127<2027:LSPAWT>2.0.CO;2

Robe, F. R., & Emanuel, K. A. (2001). The effect of vertical wind shear on radiative–convective equilibrium states. *Journal of the Atmospheric Sciences*, *58*(11), 1427–1445. https://doi.org/10.1175/1520-0469(2001)058<1427:TEOVWS>2.0.CO;2

Ruppert, J. H., & Hohenegger, C. (2018). Diurnal circulation adjustment and organized deep convection. *Journal of Climate*, *31*(12), 4899–4916. https://doi.org/10.1175/JCLI-D-17-0693.1

Sato, Y., Nishizawa, S., Yashiro, H., Miyamoto, Y., Kajikawa, Y., & Tomita, H. (2015). Impacts of cloud microphysics on trade wind cumulus: Which cloud microphysics processes contribute to the diversity in a large eddy simulation? *Progress in Earth and Planetary Science*, *2*(1), 23. https://doi.org/10.1186/s40645-015-0053-6

Satoh, M., Aramaki, K., & Sawada, M. (2016). Structure of tropical convective systems in aqua-planet experiments: Radiative-convective equilibrium versus the Earth-like experiment. *SOLA*, *12*(0), 220–224. https://doi.org/10.2151/sola.2016-044

Scotti, A., Meneveau, C., & Lilly, D. K. (1993). Generalized Smagorinsky model for anisotropic grids. *Physics of Fluids A: Fluid Dynamics*, *5*(9), 2306–2308. https://doi.org/10.1063/1.858537

Sekiguchi, M., & Nakajima, T. (2008). A k-distribution-based radiation code and its computational optimization for an atmospheric general circulation model. *Journal of Quantitative Spectroscopy and Radiative Transfer*, *109*(17–18), 2779–2793. https://doi.org/10.1016/j.jqsrt.2008.07.013

Silvers, L. G., Stevens, B., Mauritsen, T., & Giorgetta, M. (2016). Radiative convective equilibrium as a framework for studying the interaction between convection and its large-scale environment. *Journal of Advances in Modeling Earth Systems*, *8*(3), 1330–1344. https://doi.org/10.1002/2016MS000629

Tomita, H. (2008). New microphysical schemes with five and six categories by diagnostic generation of cloud ice. *Journal of the Meteorological Society of Japan. Ser. II*, *86A*, 121–142. https://doi.org/10.2151/jmsj.86A.121

Tomita, H., & Abe, K. (2000). Numerical simulation of pattern formation in the Bénard–Marangoni convection. *Physics of Fluids*, *12*(6), 1389–1400. https://doi.org/10.1063/1.870390

Tompkins, A. M., & Craig, G. C. (1998). Radiative–convective equilibrium in a three-dimensional cloud-ensemble model. *Quarterly Journal of the Royal Meteorological Society*, *124*(550), 2073–2097. https://doi.org/10.1002/qj.49712455013

Wilson, D. K. (2001). An alternative function for the wind and temperature gradients in unstable surface layers. *Boundary-Layer Meteorology*, *99*(1), 151–158. https://doi.org/10.1023/A:1018718707419

Windmiller, J. M., & Hohenegger, C. (2019). Convection on the edge. *Journal of Advances in Modeling Earth Systems*, *11*(12), 3959–3972. https://doi.org/10.1029/2019MS001820

Wing, A. A., & Cronin, T. W. (2016). Self-aggregation of convection in long channel geometry. *Quarterly Journal of the Royal Meteorological Society*, *142*(694), 1–15. https://doi.org/10.1002/qj.2628

Wing, A. A., & Emanuel, K. A. (2014). Physical mechanisms controlling self-aggregation of convection in idealized numerical modeling simulations. *Journal of Advances in Modeling Earth Systems*, *6*(1), 59–74. https://doi.org/10.1002/2013MS000269

Wing, A. A., Emanuel, K., Holloway, C. E., & Muller, C. (2017). Convective self-aggregation in numerical simulations: A review. *Surveys in Geophysics*, *38*(6), 1173–1197. https://doi.org/10.1007/s10712-017-9408-4

Wing, A. A., Stauffer, C. L., Becker, T., Reed, K. A., Ahn, M., Arnold, N. P., et al. (2020). Clouds and convective self-aggregation in a multimodel ensemble of radiative-convective equilibrium simulations. *Journal of Advances in Modeling Earth Systems*, *12*(9). https://doi.org/10.1029/2020MS002138

Yamaguchi, T., & Feingold, G. (2015). On the relationship between open cellular convective cloud patterns and the spatial distribution of precipitation. *Atmospheric Chemistry and Physics*, *15*(3), 1237–1251. https://doi.org/10.5194/acp-15-1237-2015

Yanase, T., & Takemi, T. (2018). Diurnal variation of simulated cumulus convection in radiative-convective equilibrium. *SOLA*, *14*, 116–120.

Yanase, T., Nishizawa, S., Miura, H., Takemi, T., & Tomita, H. (2020). New critical length for the onset of self-aggregation of moist convection. *Geophysical Research Letters*, *47*(16), e2020GL088763.

Yang, D. (2018). Boundary layer height and buoyancy determine the horizontal scale of convective self-aggregation. *Journal of the Atmospheric Sciences*, *75*(2), 469–478. https://doi.org/10.1175/JAS-D-17-0150.1

Yao, L., Yang, D., & Tan, Z.-M. (2021). A vertically resolved MSE framework highlights the role of the boundary layer in convective self-aggregation. *Journal of the Atmospheric Sciences*, *1*(aop). https://doi.org/10.1175/JAS-D-20-0254.1

Zhang, C. (2005). Madden-Julian oscillation. *Reviews of Geophysics*, *43*(2). https://doi.org/10.1029/2004RG000158

Figure 1.

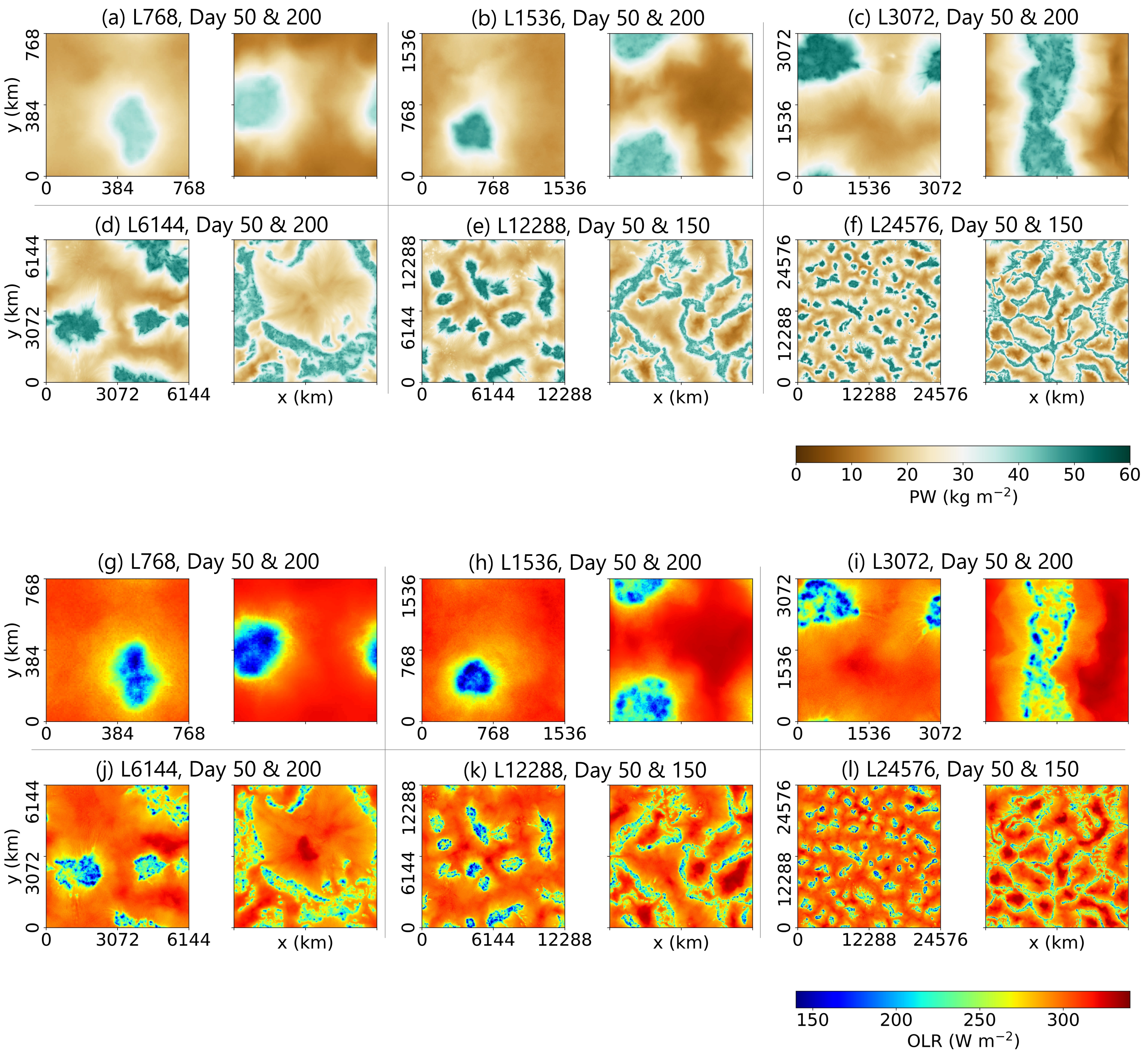

(a) L768, Day 50 & 200
(b) L1536, Day 50 & 200
(c) L3072, Day 50 & 200
(d) L6144, Day 50 & 200
(e) L12288, Day 50 & 150
(f) L24576, Day 50 & 150
y (km)
x (km)
PW (kg m^{-2})
0 10 20 30 40 50 60
(g) L768, Day 50 & 200
(h) L1536, Day 50 & 200
(i) L3072, Day 50 & 200
(j) L6144, Day 50 & 200
(k) L12288, Day 50 & 150
(l) L24576, Day 50 & 150
OLR (W m^{-2})
150 200 250 300

Figure 2.

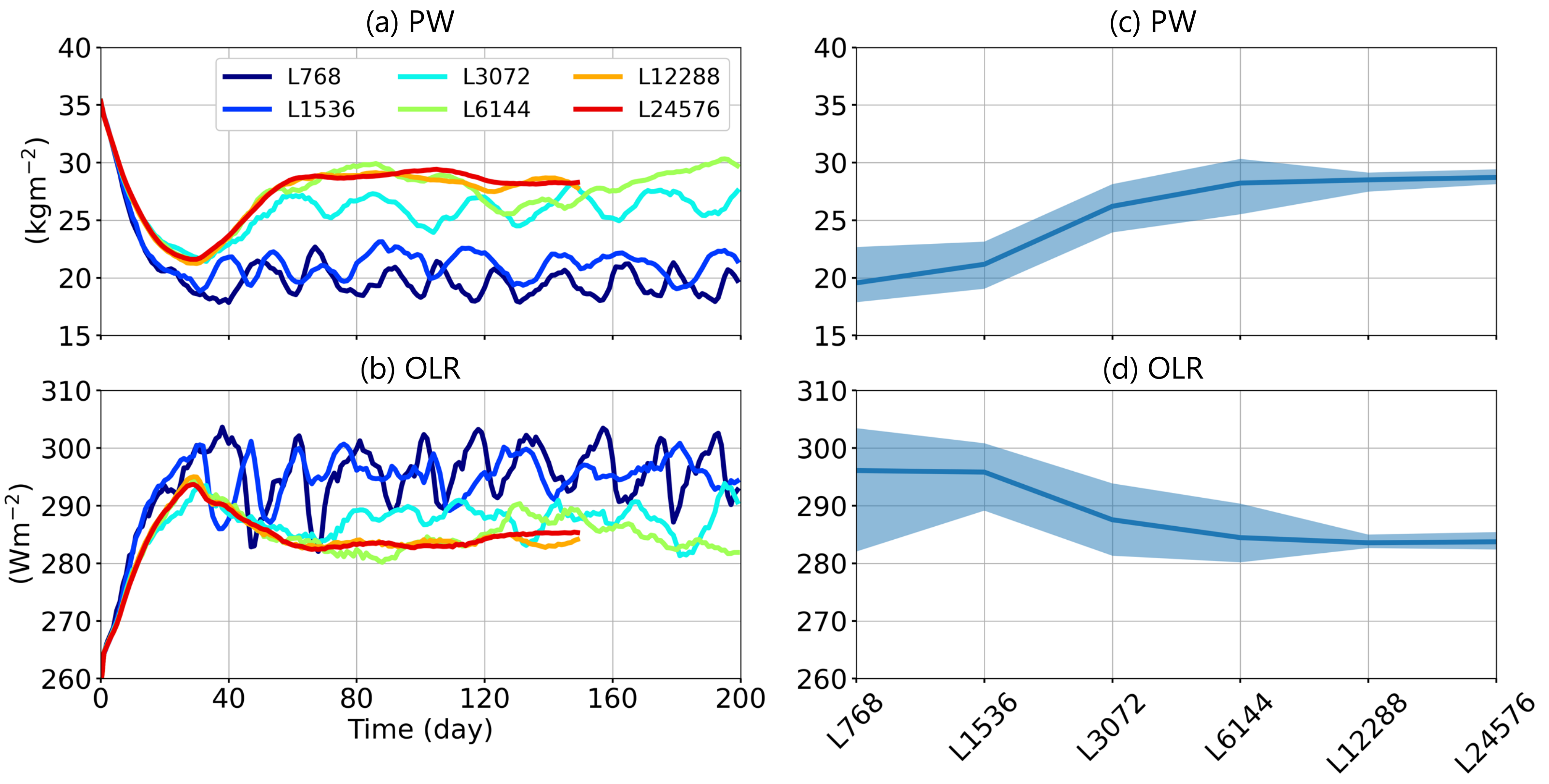

(a) PW
(b) OLR
(c) PW
(d) OLR
L768
L1536
L3072
L6144
L12288
L24576
(kgm^{-2})
(Wm^{-2})
Time (day)

Figure 3.

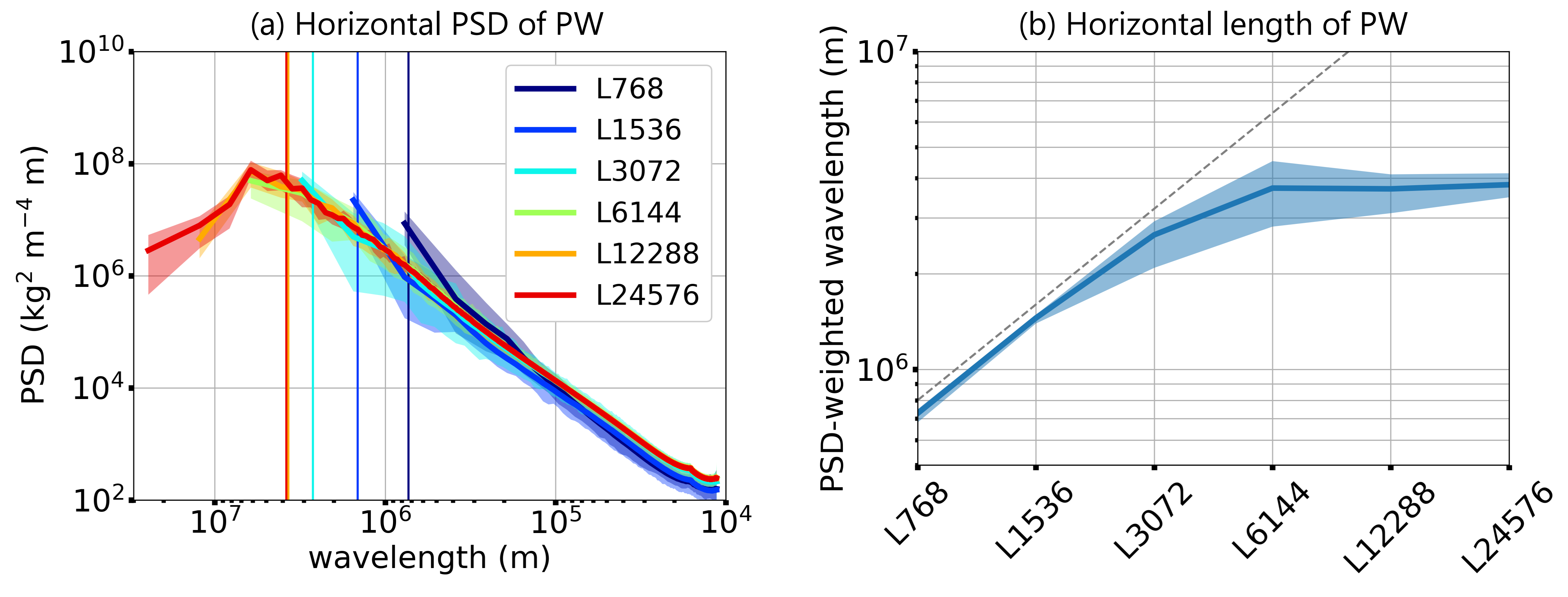

(a) Horizontal PSD of PW
PSD (kg^2 m^{-4} m)
wavelength (m)
10^{10}
10^{8}
10^{6}
10^{4}
10^{2}
10^{7}
10^{6}
10^{5}
10^{4}
L768
L1536
L3072
L6144
L12288
L24576
(b) Horizontal length of PW
PSD-weighted wavelength (m)
10^{7}
10^{6}
L768
L1536
L3072
L6144
L12288
L24576

Figure 4.

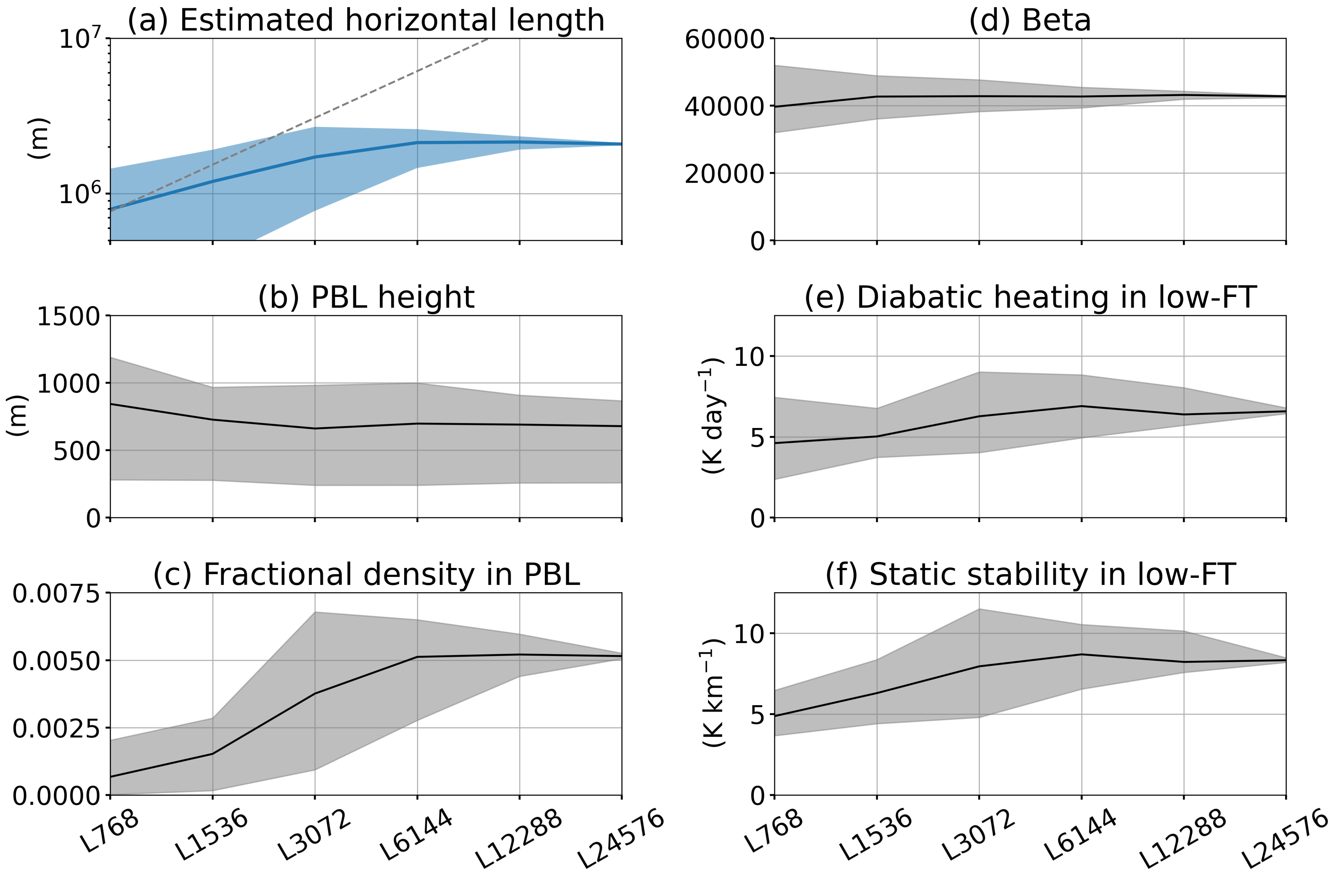

(a) Estimated horizontal length
(m)
10^7
10^6
(b) PBL height
(m)
1500
1000
500
0
(c) Fractional density in PBL
0.0075
0.0050
0.0025
0.0000
(d) Beta
60000
40000
20000
0
(e) Diabatic heating in low-FT
(K day^{-1})
10
5
0
(f) Static stability in low-FT
(K km^{-1})
10
5
0
L768
L1536
L3072
L6144
L12288
L24576